Charge transport by global protonic conductivity and relaxational dynamics over hydrogen bonds in Fe2+Fe3+3.2(Mn2+,Zn)0.8(PO4)3(OH)4.2(HOH)0.8

M. Winkler, Peter Lunkenheimer, Alois Loidl, S.-H. Park, B. Röska, M. Hoelzel

Charge transport by global protonic conductivity and relaxational dynamics over hydrogen bonds in $Fe^{2+}Fe^{3+}_{3.2}(Mn^{2+},Zn)_{0.8}(PO_4)_3(OH)_{4.2}(HOH)_{0.8}$

M. Winkler[a], P. Lunkenheimer[a], A. Loidl[a], S.-H. Park[b,*], B. Röska[b], M. Hoelzel[c]

[a] *Experimental Physics V, Center for Electronic Correlations and Magnetism, University of Augsburg, 86159 Augsburg, Germany*
[b] *Department of Earth- and Environmental Sciences, Section of Crystallography, Ludwig-Maximilians-Universität München (LMU), Theresienstr. 41C, 80333 Munich, Germany*
[c] *Heinz Maier-Leibnitz Zentrum, Technische Universität München (TUM), Lichtenbergstr. 1, 85748 Garching, Germany.*

A B S T R A C T

This study deals with the charge transport by protons over hydrogen bonds (HBs) in a rockbridgeite-type compound, $Fe^{2+}Fe^{3+}_{3.2}(Mn^{2+},Zn)_{0.8}(PO_4)_3(OH)_{4.2}(HOH)_{0.8}$. Its dielectric response in a wide frequency range of 1 Hz – 3 GHz from 30 K to 500 K can be traced back to structural properties of this phosphatic oxyhydroxide, revealed by Rietveld refinements using neutron powder diffraction data. The probable charge transport paths for protons are proposed, based on the honeycomb-like distribution of their neutron scattering length densities reconstructed by the Maximum-Entropy Method. Two distinctly decoupled proton dynamic processes occur in this system: at high temperatures, global protonic transport is thermally activated over an energy barrier (E_B) of 0.49 eV, showing a dc conductivity (σ_{dc}) value of about $10^{-4}\ \Omega^{-1}\ cm^{-1}$ at 500 K. The temperature-dependency of σ_{dc} becomes weaker at decreased temperatures, indicating the possible onset of proton tunneling-dominated charge transport. At low temperatures, relaxational proton hopping within double-well potentials in HBs is thermally activated with $E_B = 0.62$ eV. An extremely fast relaxation time of ~50 ps at 250 K continuously slows down to ~1 ms at 150 K, pointing to the approach of an orientational proton-glass state at about 125 K. Isosurfaces of bond valence energy landscape maps of H^+ at 0.49 eV clearly evidence the honeycomb-shaped route for the protonic conductivity at 393 K.

1. Introduction

Transition metal oxyhydroxide minerals [1] are interesting matrices for diverse magnetic spin orders, intervalence charge transfer [2], and protonic charge transport. However, only a small part of such interesting structure-related properties of this type of structures are unveiled. Our recent study of rockbridgeite ($Fe^{2+}Fe^{3+}_{3.2}(Mn^{2+},Zn)_{0.8}(PO_4)_3(OH)_{4.2}(HOH)_{0.8}$) has predicted fast proton dynamics, based on an unusual dramatic increase of the di-electric permittivity above about 250 K [3]. A similar phosphatic oxy-hydroxide, Mn-hureaulite ($Mn^{2+}_5(PO_4)_2(PO_3(OH))_2(HOH)_4$) shows fast site-exchanging protons between semihelical hydrogen bond (HB) chains with a bulk dc conductivity value of $4.5 \times 10^{-5}\ \Omega^{-1}\ cm^{-1}$ at 498 K determined on a powder sample [4]. A common interesting feature of rockbridgeite- and hureaulite-type compounds with alkali sulphatic and arsenatic oxides known as superprotonic conductors [5,6] is the presence of fast protonic motions over their HB networks. Thus, a strong correlation with fast protonic dynamic disorder caused by collective reorientation of the octahedral-tetrahedral (OT) framework polyhedra in phosphatic oxyhydroxides is expected [7]. Such lattice dynamics are accompanied by the realization of dynamically disordered HB networks (DDHBN) as a basis of the superprotonic conductivity, as observed in sulphatic and arsenatic oxides ([5,7] and literature therein). In this context, the determination of the HB network of rockbridgeite [3] has enhanced our interest in the elucidation of its protonic charge transport mechanism.

The rockbridgeite topology is a mixed OT framework of Fe$(O,OH,HOH)_6$ and $P(O,OH)_4$ entities with OH and HOH ligand groups (no zeolitic water) [8]. The octahedral moieties in rockbridgeite-type structures consist of $[Fe1(O,OH)_6]$, $[Fe2(O,OH,HOH)_6]$, and $[Fe3(O,OH,HOH)_6]$ with three independent sites Fe1, Fe2, and Fe3 for Fe^{3+} and (Fe, Mn, Zn)$^{2+}$, respectively. Fe2-Fe1-Fe2 octahedra are connected via faces to form *h-clusters* [9] being edge-linked to form infinite chains in [001] (Fig. 1a). *h*-clusters are linked to each other via alternatingly occupied Fe3 octahedral doublets in [100]. One of the relevant structural features in this compound is the static disorder of
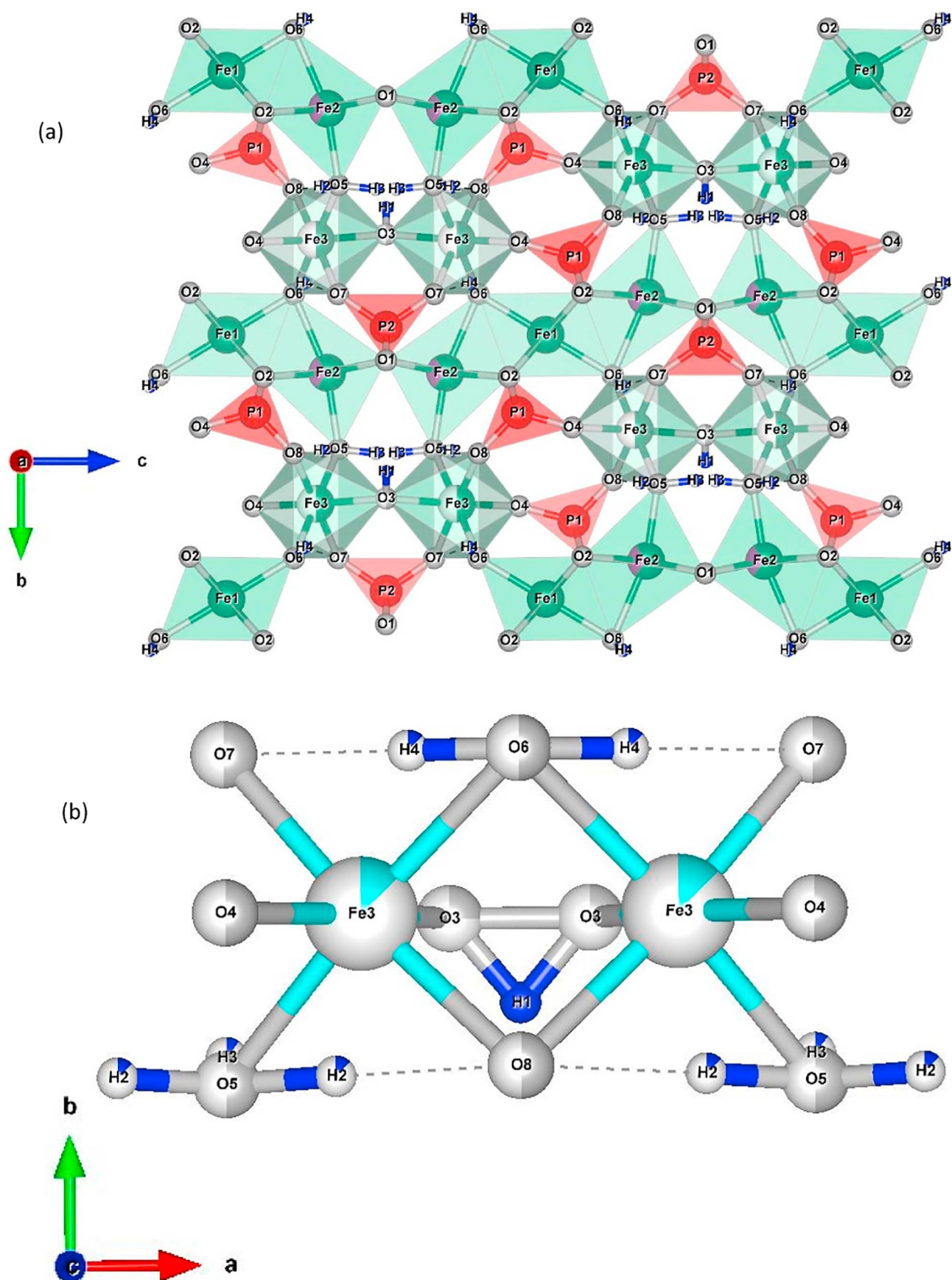
Fig. 1. a) The topology of rockbridgeite-type structures consists of Fe(O,OH,HOH)$_6$ octahedra and P(O,OH)$_4$ tetrahedra. The so-called *h-cluster* is made of a face-sharing [Fe2(O,OH,HOH)$_6$]-[Fe1(O,OH)$_6$]-[Fe2(O,OH,HOH)$_6$] unit; b) An alternatingly half-occupied O3H1 and Fe3(O,OH,HOH)$_6$ results in the static disorder in their chains parallel to the *a* axis.

2
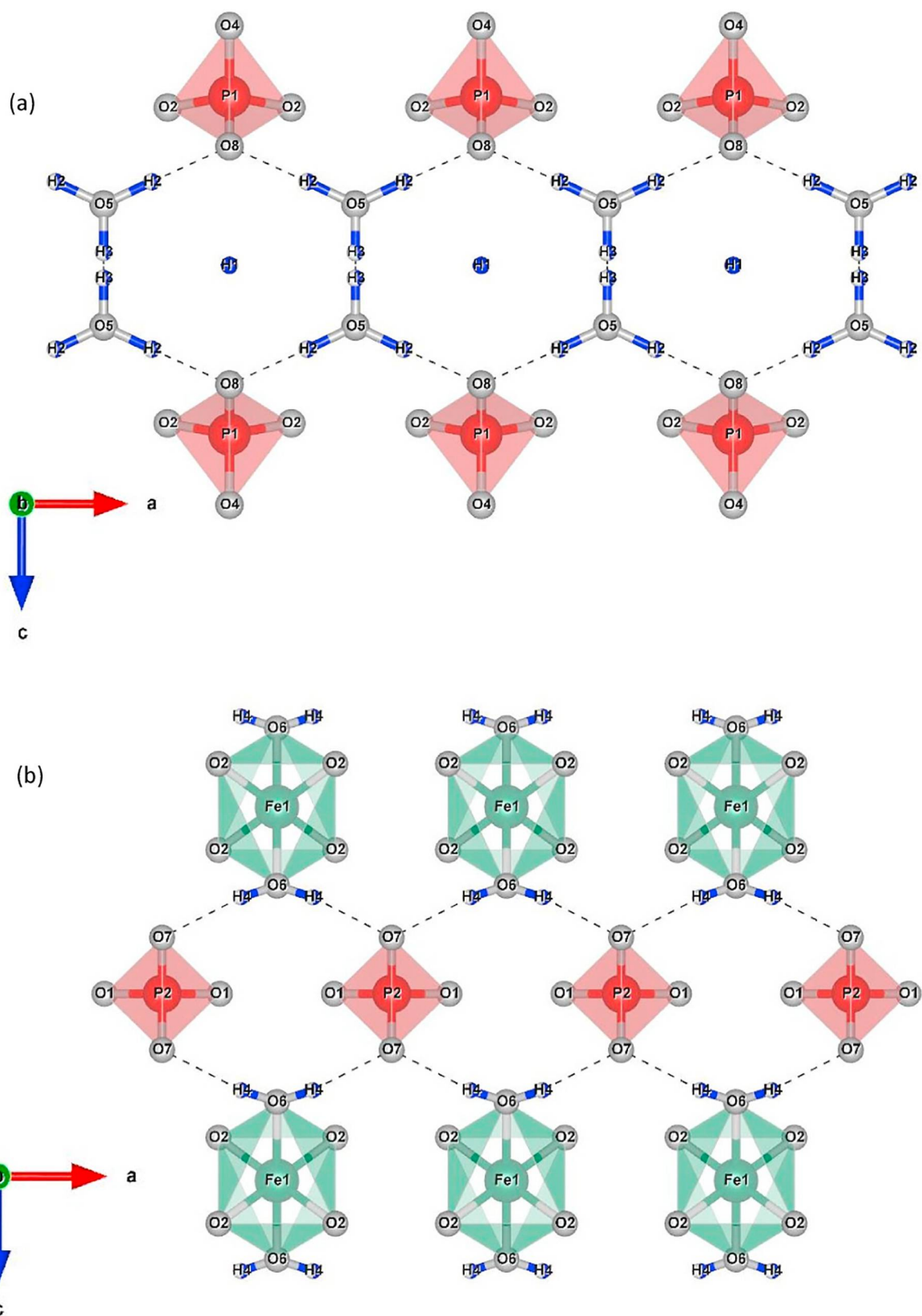
Fig. 2. The hydrogen bond network HB-I in rockbridgeite is a honeycomb-like network over the statistically occupied split sites H3 (a). A double-chain HB network, HB-II (b) runs parallel to HB-I in the (**a-c**) plane.

alternatingly half-occupied O3H1-Fe3O$_6$ chains (Fig. 1b). As the structure exhibits 2-dimensional (2D) honeycomb-like chains of HBs (named HB-I, dashed lines in Fig. 2a) running parallel to another 1D HB

chain (named HB-II, Fig. 2b) along the crystallographic **a** axis, fast protonic diffusion is suggestive in this OT framework [3]. Here, several questions are to be answered with respect to proton motions, such as: 1)

length and time scales in the proton conduction process; 2) the routes of long-range and short-range protonic dynamics; 3) the correlation of protonic motions with lattice dynamics. The present study presents the *true* DDHBN in rockbridgeite, based on Rietveld refinements, the maximum-entropy method (MEM), and bond valence energy landscape (BVEL) with high-resolution neutron powder diffraction (HRNPD) data at 393 K. The obtained relevant features are compared with those from an analyses of HRNPD data at 298 K reported in [3]. Moreover, we directly detect the protonic dynamics by dielectric measurements from 1 Hz to 3 GHz in a temperature range of 30–500 K and relate the results to the deduced structural properties of this material.

2. Experimental

2.1. Data collection and analyses of HRNPD at 393 K

A 5 g powder sample was prepared with the same batch mineral species rockbridgeite reported in [3]. HRNPD data collection was carried out with a constant wavelength of 1.5482 Å using a Ge(551) monochromator at the instrument SPODI at FRM II, Garching, Germany [10]. The powdered sample was packed within a silica glass tube to be mounted within a Nb high-temperature oven set at 393 K. A series of HRNPD data sets was collected by 80 vertically position-sensitive detectors with 300 mm-high collimators in a 2θ-range of 0.95°–153.9° with a step width of 0.05° and added up to ensure a high counting statistic. The program package Jana2006 [11] was used for Rietveld refinements with the starting model at 298 K from our recent study [3]. As reported in the previous study, the HRNPD patterns exhibit extremely high background mainly due to inelastic scattering from protons in OH and HOH groups. Therefore, atomic displacements (ADPs) were treated only isotropically due to their correlation with background parameters.

To access protons over the DDHBN, isosurface maps of coherent neutron scattering lengths (Coh_b) densities were reconstructed by MEM in order to overcome termination problems and failed determination of anharmonic ADPs for mobile protons. MEM calculations on HRNPD data iteratively determine the maximum entropy, i.e. the discrepancy between the nuclear density and a trial nuclear density under constraints using Lagrange multipliers [12]. In this study, MEM calculations were performed with an option for optimization algorism '*Limited-memory Broyden-Fletcher-Goldfarb-Shannon (L-BFGS)*' [13] embedded in the program Dysnomia [14] based on 726 and 740 structure factors from Rietveld analyses with 298 K [3] and 393 K HRNPD [the present study], respectively. In addition, using the refined structure models of the title compound as input, BVEL maps [15,16] were calculated using the bond valence parameters [17] with the BondStr interface of the FullProf suite [18]. The program VESTA [19] was applied to visualize structure models and MEM and BVEL maps.

2.2. Dielectric measurements

For dielectric measurements, contacts of silver paint were applied to opposite faces of a platelet-shaped specimen which was cut from a fibrous rockbridgeite crystallites mass. Measurements at frequencies between 1 Hz and several MHz and temperatures between 30 K and 500 K were performed using a frequency-response analyzer (Novocontrol Alpha analyzer). Below room temperature, additional high-frequency measurements were carried out at the range from 1 MHz to 3 GHz employing an impedance analyzer (Keysight E4991B) using an *I-V* coaxial technique. For this purpose, the sample was mounted at the end of a coaxial line, bridging the inner and outer conductor [20]. For cooling and heating a closed-cycle refrigerator (CTI Cryogenics Cryodyne) and a N_2-gas cryostat (Novocontrol Quatro) were used.

3. Results and discussion

3.1. Structure refinements on HRNPD data at 393 K

Rietveld refinements were straightly conducted in the space group symmetry *C*mcm with 393 K HRNPD data with the model refined with 298 K HRNPD reported in [3]. Reflections of Nb foil (heat element) are seen in the collected HRNPD pattern, and hence Nb was treated as the second phase with a preferred orientation, (213) at 122.075°(2θ). A mass ratio of 0.984(1): 0.016(1) for the main phase to Nb resulted from the last cycle of Rietveld calculations. The lattice parameters a = 5.1806(3) Å; b = 13.9820 (10) Å; c = 16.9100(19) Å refined for the main phase at 393 K agree with thermal expansion obviously occurring in the *a* and *c* directions but a slight contraction in *b* when comparing those at 298 K [3]. Experimental and Rietveld refinement parameters are summarized in Table 1.

In the whole structure refinement cycles, all occupancy parameters (Occ) were fixed to those of the starting model while simultaneously refining profile parameters, positions, and isotropic ADPs for all sites. Atomic parameters of a static disorder site M^{2+} cations, Fe2 are constraint with an occupation ratio of Fe: Mn: Zn = 61%: 29%: 10%, based on chemical analyses and Mössbauer spectra given in the previous report [3]. The refined atomic parameters for $Fe^{2+}Fe_{3.2}^{3+}(Mn^{2+},Zn)_{0.8}(PO_4)_3(OH)_{4.2}(HOH)_{0.8}$ at 393 K are given in

Table 1
Experimental and Rietveld refinement parameters of HRNPD.

Radiation source/ wavelength	Neutron/ 1.5482 Å
Temperature	393 K
Structural formula	$Fe^{2+}Fe_{3.2}^{3+}(Mn^{2+},Zn)_{0.8}(PO_4)_3(OH)_{4.2}(HOH)_{0.8}$
Formula units (Z)	4
Density (theoretical)	3.646 g/cm³
Space group symmetry	*C*mcm (# 63)
Lattice parameters	a = 5.1806 (3) Å
	b = 13.9820 (10) Å
	c = 16.9100 (10) Å
Unit cell volume	1224.8(2) Å³
Weighted residual profile (wRp) value	0.96%
Relative phase amounts in mass	Rockbridgeite: Nb foil = 0.984(1): 0.016(1)
Goodness-Of-Fit (GOF)	2.32

Table 2
Atomic positional parameters with occupancy (**Occ**), site multiplicity (**M**), and isotropic ADPs (U_{iso}), resulted from Rietveld refinements with HRNPD data at 393 K (SG: *C*mcm).

Site	Type	Occ	M	Atomic coordinate			U_{iso} [Å²]
				x	y	z	
Fe1	Fe	1	0.25	0	0	0	0.016(1)
Fe2	Fe	0.61	0.5	0	0.0719(5)	0.1576(4)	0.029(2)
	Mn	0.29					
	Zn	0.10					
Fe3	Fe	0.5	1	0.2331(9)	0.3200(4)	0.1396(2)	0.012(1)
P1	P	1	0.5	0.5	0.1473(4)	0.0441(3)	0.011(1)
P2	P	1	0.25	0	0.4856(7)	0.25	0.025(2)
O1	O	1	0.5	0.2514(12)	0.5483(4)	0.25	0.021(1)
O2	O	1	1	0.2546(9)	0.0796(3)	0.0576(2)	0.021(1)
O3	O	0.5	0.5	0.3735(18)	0.3098(9)	0.25	0.017(2)
O4	O	1	0.5	0.5	0.1754(4)	0.9583(3)	0.017(1)
O5	O	1	0.5	0	0.2168(4)	0.1756(3)	0.017(1)
O6	O	1	0.5	0.5	0.4234(5)	0.1053(3)	0.022(1)
O7	O	1	0.5	0	0.4231(4)	0.1748(3)	0.015(1)
O8	O	1	0.5	0.5	0.2248(4)	0.1049(3)	0.019(1)
H1	H	1	0.25	0.5	0.2596(18)	0.25	0.078(6)
H2	H	0.5	1	0.3088(18)	0.2802(9)	−0.1480(7)	0.027(3)
H3	H	0.4416	0.5	0	0.2240(17)	0.2341(12)	0.073(10)
H4	H	0.5	1	0.6566(17)	0.4024(8)	0.1209(7)	0.020(3)

4
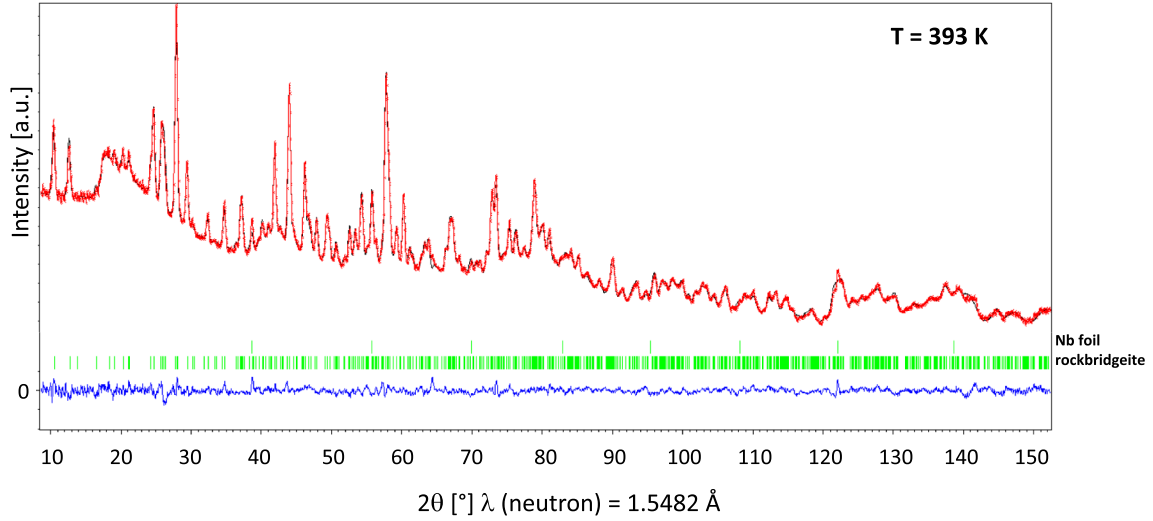
Fig. 3. Graphic presentation of Rietveld calculation (black line) with observed (red +) HRNPD pattern at 393 K. Short green bars indicate the positions of rockbridgeite and Nb reflections. The flat difference profile between observed and calculated intensities plotted at the bottom is in accord with the low residual value GOF (Goodness of fit) = 2.32. (For interpretation of the references to colour in this figure legend, the reader is referred to the web version of this article.)

Table 2. A good agreement between observed and calculated HRNPD patterns is graphically demonstrated in Fig. 3.

3.2. Hydrogen bonds in $Fe^{2+}Fe_{3.2}^{3+}(Mn^{2+},Zn)_{0.8}(PO_4)_3(OH)_{4.2}(HOH)_{0.8}$ at 393 K

As shown in Table 3, three independent sites for protons (H2, H3, and H4) are involved in building up both honeycomb chains (HB-I, Fig. 2a) and double zigzag chains of HBs (HB-II, Fig. 2b). HB-I and HB-II run commonly parallel to the **a** axis without interruption. It is worth noting that a very short, almost stretched HB is found over the split H3 sites which are available for both static and dynamic disorder of H^+, i.e. d(O5-H3⋯O5) = 2.52(1) Å; ∠(O5-H3⋯O5) = 170(2)° at 393 K. The distance d(H3−H3) = 0.54(5) Å at 393 K is fairly shorter, compared to d(H3-H3) = 0.64(1) Å at 298 K [3]. The configuration of this short HB in variation of temperature is compiled in Table 4: in spite of a faint difference of 0.02(2) Å of the HB distance d(O5-H3⋯O5) between 20 K and 393 K, this HB becomes more stretched and more symmetrical at both 20 K and 393 K than that at 298 K. The low temperature case can be explained by a temperature-induced lock-in effect on H^+ in the HB (O5-H3-O5). Another interesting feature in this short HB is drawn at elevated temperatures from RT with the values for ∠(O5-H3⋯O5) = 158(2)° at 298 K and 170(2)° at 393 K along with the decreasing difference between d(O5-H3) and d(H3⋯O5) from 0.64 Å at 298 K to 0.56 Å at 393 K. This shortening-stretching of the HB (O5-H3⋯O5) is hence thermally induced and indicates a local dynamic disorder over the static disorder site H3.

On the other hand, the site H1 is included in neither HB-I nor HB-II, as H1 is located within large cages, available for a OH group dangling in either way at two alternatingly half occupied $Fe3O_6$ octahedra

(Fig. 1b). Nonetheless, for the global charge transport in rockbridgeite, it is critical to inherit protons at H1 sites because the *true* DDHBN cannot be realized without H1 over which long-range dynamical disorder of protons proceeds (see the next section). This means the site H3 over which the honeycomb chains of HB-I can be framed, as shown in Fig. 2a, does not belong to the *true* DDHBN. The location of the *true* DDHBN is exactly in between two neighbouring honeycombs of HB-I. This is clearly seen when plotting the neutron scattering length distribution of H^+ in the (**a-c**) plane (Fig. 4a), as described in detail below.

3.3. Neutron scattering length distribution around protons from MEM calculations

The reconstruction of density distribution of the coherent neutron scattering length of H ($Coh_b(H)$) using MEM revealed a continuous honeycomb-like distribution of $Coh_b(H)$, as highlighted in Fig. 4a with solid lines across the H1 sites. Diffuse isosurfaces of protons at a cut-off of −0.05 fm/Å³ are continuously connected over H1 sites, but displaced from the original honeycomb-shaped HB-I. This features a honeycomb-like route for hopping protons, displaced exactly a half unit cell along the **a** axis from the honeycomb network HB-I. In contrast, the $Coh_b(H)$ density is locally concentrated merely between double HB chains of HB-II (Fig. 4b). Hence, the honeycomb-like density distribution of $Coh_b(H)$ can be considered as the trace of *true* DDHBN. It is in fact reasonable for H^+ of OH and HOH ligand groups to be mobile readily perpendicular to strongly aligned HBs. In other words, the pathway for the long-range charge transport in this system is not directly along the HB-I network but detoured in between over H1 sites in the (**a-c**) plane. In turn, the two statistically occupied H3 sites belonging to the route of HB-I are not directly involved in the *true* DDHBN available for long-range charge transport at 393 K. Furthermore, the isolated $Coh_b(H)$ density is concentrated exactly in the middle of two split H3 sites at 393 K (Fig. 4a), which indicates a fast hopping of H^+ back and forth between two split H3 sites.

At 298 K, the reconstructed density distribution of $Coh_b(H)$ around HB-I differs from that at 393 K, as shown in Fig. 5: site-exchanging protons are adumbrated rather between H3 and H2, than between H1 and H2 (solid circle lines in green). Furthermore, there is a narrowing of $Coh_b(H)$ density in the middle of two H3 sites (solid red circle). This reflects the distance d(H3-H3) longer at 298 K than at 393 K (Table 4). From these observations, one can conclude that H3 sites mainly provide pathways for locally site-exchanging protons.

Table 3
Geometric parameters of HBs in $Fe^{2+}Fe_{3.2}^{3+}(Mn^{2+},Zn)_{0.8}(PO_4)_3(OH)_{4.2}(HOH)_{0.8}$ at 393 K, showing a very short HB length of 2.52(1) Å for the almost stretched HB (O5-H3⋯O5).

HBs	d(O-H) Å	d(H⋯O) Å	d(O-H⋯O) Å	∠(O-H⋯O) [°]
O5-H2⋯O3	1.10(1)	2.34(1)	2.65(1)	94(1)
O5-H2⋯O8	1.10(1)	1.76(1)	2.86(1)	179(1)
O5-H3⋯O3	0.99(2)	2.29(2)	2.65(1)	100(1)
O5-H3⋯O5	0.99(2)	1.53(2)	2.52(1)	170(2)
O6-H4⋯O4	0.90(1)	2.48(1)	3.13(1)	129(1)
O6-H4⋯O7	0.90(1)	2.02(1)	2.84(1)	151(1)

Table 4

The short hydrogen bond in $Fe^{2+}Fe^{3+}_{3.2}(Mn^{2+},Zn)_{0.8}(PO_4)_3(OH)_{4.2}(HOH)_{0.8}$ at 393 K [this work], compared with those at 20 K and 298 K [3].

| T [K]	d(O5-H3) [Å]	d(H3···O5) [Å]	Δ|d(H3···O5) -d(O5-H3)| [Å]	d(O5-H3···O5) [Å]	∠(O5-H3···O5) [°]
20	1.280(1)	1.28(1)	0	2.54(1)	166(3)
298	0.97(2)	1.61(2)	0.64	2.53(1)	158(2)
393	0.99(2)	1.53(2)	0.56	2.52(1)	170(2)

3.4. Dielectric measurements

Fig. 6a shows the temperature dependence of the dielectric constant ε' as measured for various frequencies of the applied field. At low temperatures, $\varepsilon'(T)$ is nearly constant and has a moderate value of about 18, as seen in Fig. 6a. No anomaly is detected at the transition into the ferrimagnetic state occurring at about 82 K [3], i.e. there is no coupling of dielectric and magnetic properties in this material. With increasing temperature, $\varepsilon'(T)$ exhibits a strong increase whose onset depends on the measurement frequency. This is reminiscent of a dramatic increase of $\varepsilon'(T)$, measured in the previous study at a single frequency of 1 kHz only, as mentioned in the Introduction [3]. For low frequencies and high temperatures, $\varepsilon'(T)$ reaches very large values beyond 10^4. Overall, such behavior is typical for electrode-polarization effects (sometimes termed "blocking electrodes") as often found for ionic conductors [21]. It arises when the frequencies are such low that the charge carriers arrive at the electrodes before the polarity reverses. Then further ion motion is blocked and so-called space-charge regions are formed. The emerging thin insulating surface layers can give rise to dielectric constants of apparently "colossal" [22] magnitude and non-intrinsic Maxwell-Wagner relaxations [21]. Indeed, the step-like increase of $\varepsilon'(T)$ revealed by Fig. 6a, shifting to higher temperatures with increasing frequency, reminds of the typical behavior of a relaxation process [23,24].

Fig. 6b shows the temperature-dependent real part of the conductivity σ' for different frequencies. As σ' and the dielectric loss ε'' are related via $\sigma' \propto \varepsilon''\nu$, the $\sigma'(T)$ curves in Fig. 6b also provide information on the temperature dependence of ε''. With decreasing temperature, $\sigma'(T)$ shown in Fig. 6b first follows a decrease that is common for all frequencies before it crosses over into weaker temperature dependence. The crossover temperature becomes smaller for lower frequencies. This common decrease of $\sigma'(T)$ can be identified with the dc conductivity σ_{dc}, which is characterized by a frequency-independent σ' at low frequencies [25].
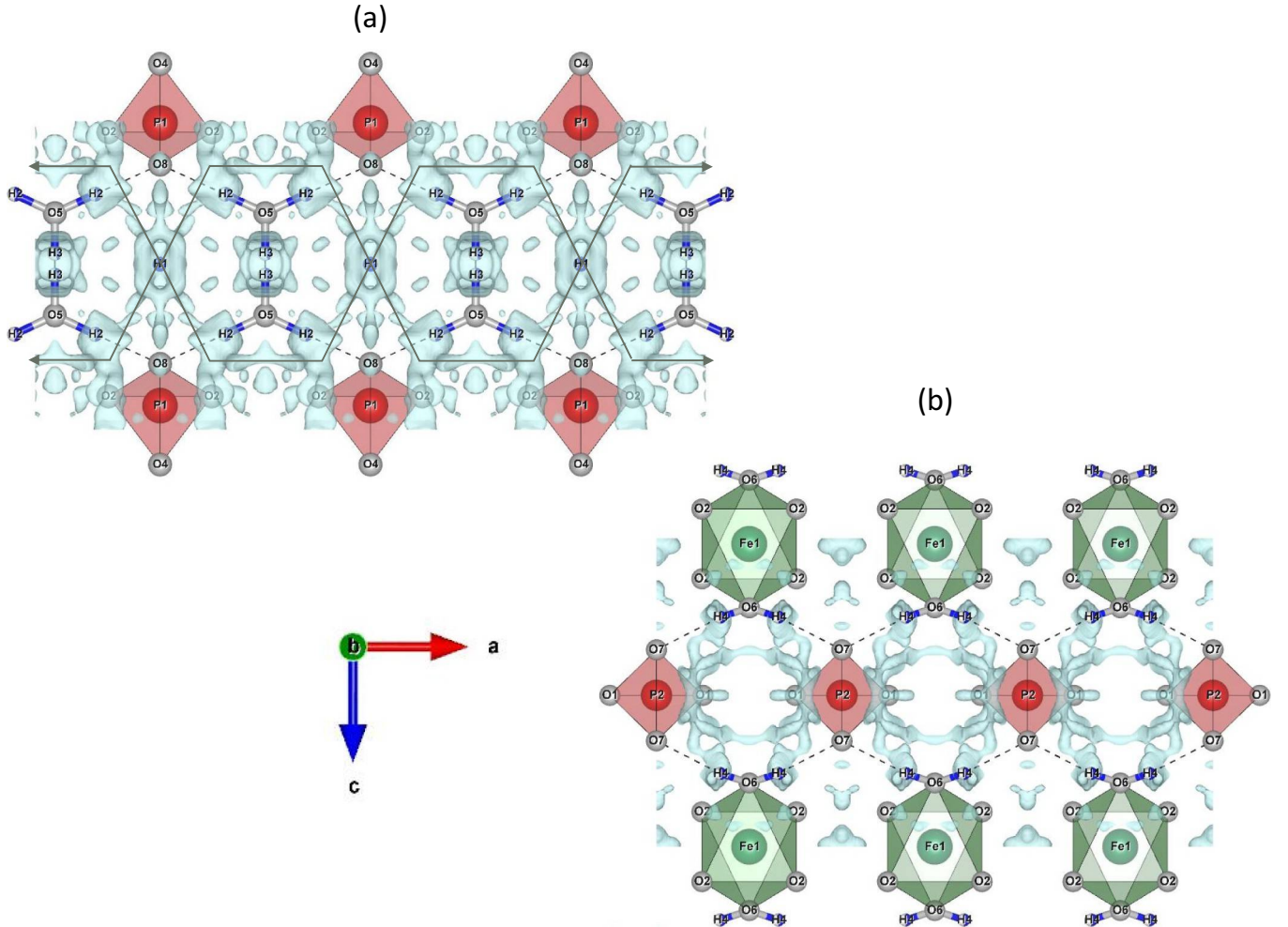
Fig. 4. Neutron scattering length density distribution of protons at 393 K around HB-I (a) and HB-II (b) obtained by MEM calculations at an isosurface level of -0.05 fm/Å^3. The route highly possible for a long-range order dynamic of protons is across HB-I over H1 sites, as highlighted in solid green lines. (For interpretation of the references to colour in this figure legend, the reader is referred to the web version of this article.)
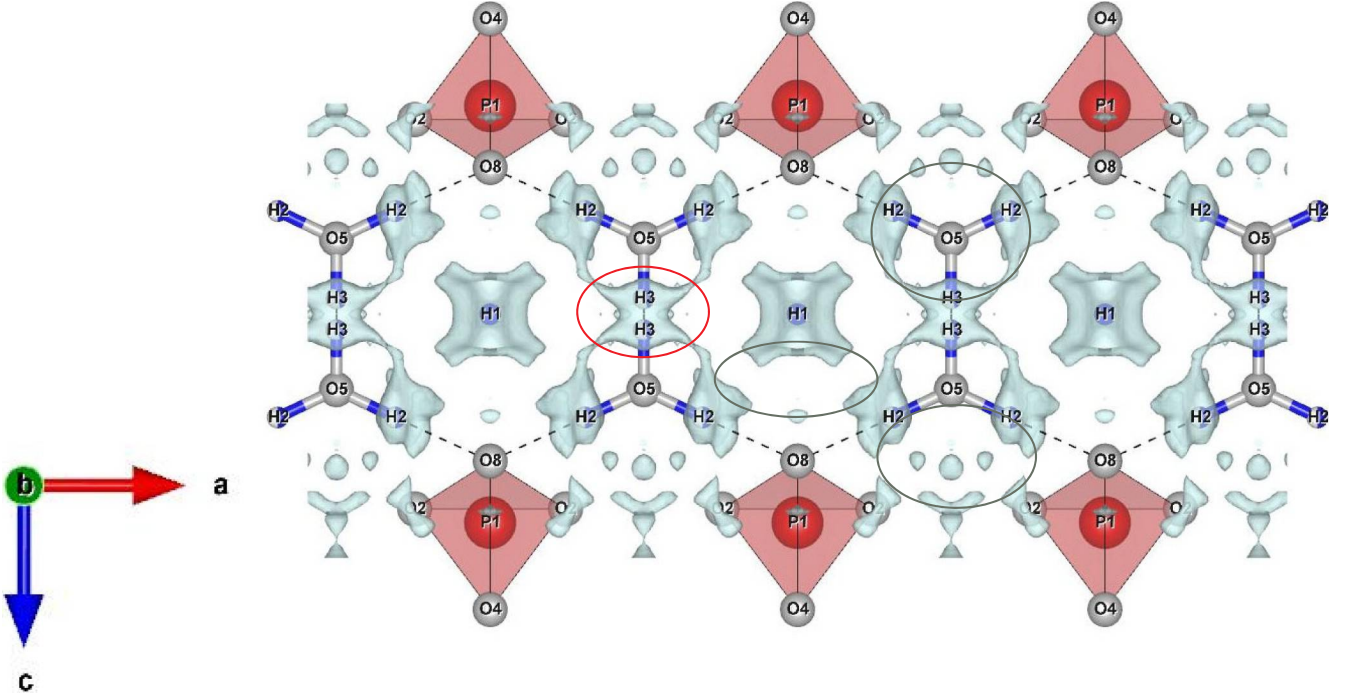
Fig. 5. Neutron scattering length density distribution of protons at 298 K around HB-I obtained by MEM calculations at an isosurface level of -0.5 fm/Å^3 adumbrates vehicle-likely site-exchanging protons along H3-H2-H2 around O5 (as highlighted by green circles), as well as fast local hopping over the short split sites H3-H3 (solid red circle). There is a narrowing of $Coh_b(H)$ density in the middle of two H3 sites. These locally limited fast dynamics of protons can contribute to charge transport at low thermal activation near RT (this 298 K HRNPD data was collected in the previous study for Rietveld analysis, as reported in [3]). (For interpretation of the references to colour in this figure legend, the reader is referred to the web version of this article.)
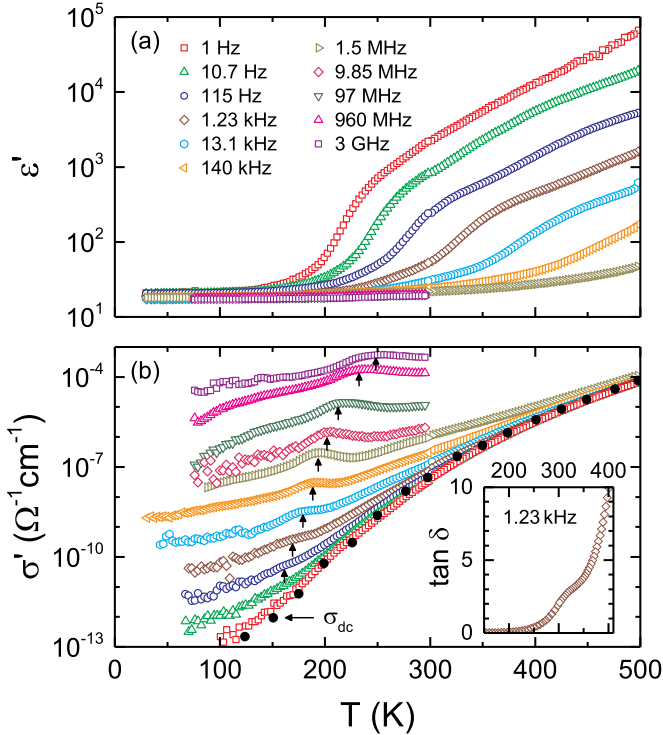
Fig. 6. Temperature dependence of the dielectric constant ε' (a) and the conductivity σ' (b) as measured at various frequencies of the applied electric field. The closed circles in frame (b) show the dc conductivity $\sigma_{dc}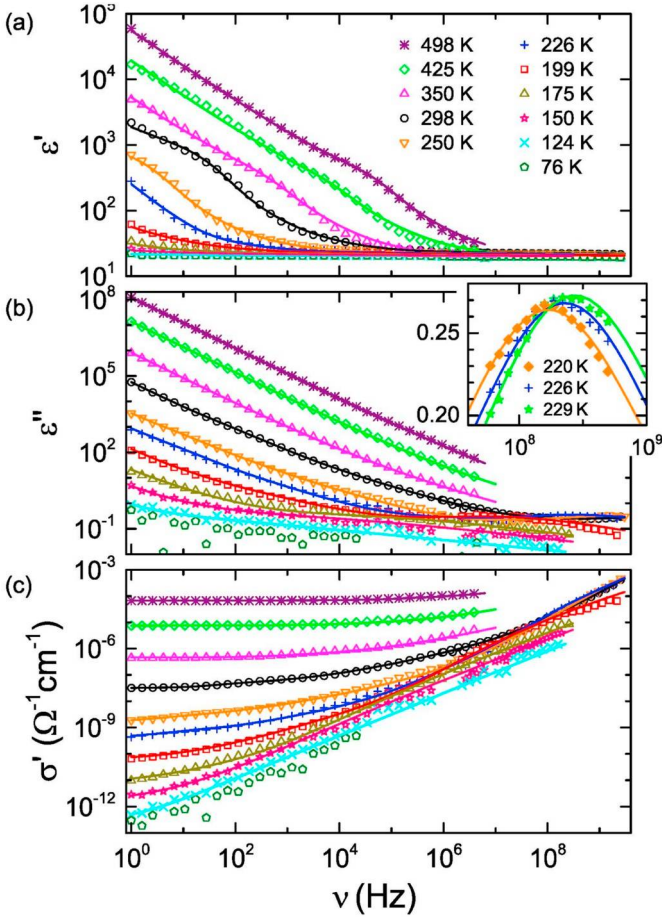$ as deduced from the fits of the frequency-dependent data. The arrows indicate the approximate positions of the relaxation peaks in $\sigma'(T)$. The inset shows the temperature dependence of the loss tangent for 1.23 kHz (cf. Fig. 11b in ref. [3]).

At temperatures below the mentioned crossover, $\sigma'(T)$ exhibits strong dispersion effects and a peak (indicated by the arrows in Fig. 6b) that shifts to lower temperatures with decreasing frequency. Such peaks in $\sigma'(T)$ [and thus in $\varepsilon''(T)$] are characteristic features of relaxational processes, typically pointing to reorientational motions of dipolar degrees of freedom that continuously slow down when temperature decreases [23,24,26]. Within this scenario, for a given measurement frequency ν the peaks occur when the temperature-dependent relaxation time $\tau(T)$ matches the condition $\tau(T_p) = 1/(2\pi\nu)$, with T_p denoting the peak temperature. It should be noted that the observed peak temperatures clearly do not coincide with the temperatures of the step-like increase observed in $\varepsilon'(T)$ (Fig. 6a), i.e. these peaks are of intrinsic origin and not related to the non-intrinsic Maxwell-Wagner relaxation caused by electrode polarization discussed above.

The inset of Fig. 6 shows the temperature dependence of the loss tangent (i.e. tan $\delta = \varepsilon''/\varepsilon'$) for 1.23 kHz. The found behavior is in reasonable agreement with a corresponding plot of tan δ at 1 kHz, reported in [3] for a different batch sample of the same origin. The general tendency of the loss tangent to increase with rising temperature mainly mirrors the strong growth of $\sigma' \propto \varepsilon''\nu$ with temperature as revealed by Fig. 6b. In addition, a peak is superimposed to this increase, located somewhat above 300 K. A corresponding feature is also faintly visible in the logarithmic plot of σ' shown in Fig. 6b. This loss peak occurs at a similar temperature as the strong step in $\varepsilon'(T)$ discussed above and obviously arises from the same phenomenon, the Maxwell-Wagner relaxation due to electrode polarization [21].

Fig. 7 demonstrates the frequency dependence of ε' (a), ε'' (b), and σ' (c) for various temperatures. The very high dielectric-constant values revealed at low frequencies and high temperatures (Fig. 7a) again point to the dominance of non-intrinsic electrode-polarization contributions in this region. To check for this notion, we made two room-temperature measurements of a sample before and after reducing its thickness from 1 to 0.3 mm by polishing (not shown). While we found a good agreement of the measured ε' spectra at frequencies above about 1 kHz, at

Fig. 7. Frequency dependence of ε' (a), ε'' (b) and σ' (c) at various temperatures. The solid lines are fits as described in the text. $\varepsilon'(\nu)$ and $\varepsilon''(\nu)$ were simultaneously fitted and the σ' fit curve calculated from ε''. For the high-frequency results, the zoomed view of the inset demonstrates the presence of a relaxation peak in $\varepsilon''(\nu)$, which was fitted by the Havriliak-Negami function (lines).

lower frequencies clear deviations were detected, proving the non-intrinsic, surface-related nature of the measured dielectric response in this region [27,28].

In $\sigma'(\nu)$ (Fig. 7c), a well-pronounced frequency-independent plateau shows up at low frequencies, indicating dc charge transport as already suggested in the discussion of Fig. 6 [25]. Via the relation $\varepsilon'' \propto \sigma'/\nu$, it leads to the observed continuous increase of ε'' with decreasing frequency revealed in Fig. 7b at low frequencies. Close to 500 K, the dc conductivity (σ_{dc}) estimated from the plateau in $\sigma'(\nu)$ reaches rather considerable values of about 10^{-4} Ω^{-1} cm^{-1}. Based on the electrode-polarization effects observed in ε', the detected conductivity is explained most likely by the motion of ionic charge carriers, i.e. protons in this system.

In principle, relaxational dynamics as evidenced by the peaks in the temperature-dependent σ' plot of Fig. 6b should also lead to peaks in the frequency dependence of the dielectric loss [23,24,26]. Indeed, for the lower temperatures, where the superimposed conductivity contribution is less relevant, indications of broad loss peaks are revealed in Fig. 7b (e.g., at about 10^7 Hz for 199 K). However, one should be aware that, depending on frequency range and temperature, the data in this low-loss region are partly hampered by the resolution limit of the used experimental setups leading to excessive data scatter. Nevertheless, in certain regions rather well-defined loss peaks are observed (see, e.g. inset of Fig. 7b). This allows for the determination of the relaxation time, either by reading off the peak frequency ν_p [via the relation $\tau = 1/(2\pi\nu_p)$] or by performing fits with the Havriliak-Negami [29] or

Cole-Cole [30] equations, which are well-established for an empirical description of relaxation peaks [23,24].

To fit the complete spectra of Fig. 7, we have modeled the electrode contributions by a distributed RC equivalent-circuit, assumed to be connected in series to the sample [21]. As previously demonstrated, this approach is able to reasonably describe such effects in various materials, including ionic conductors [21,27,28,31]. The intrinsic sample properties were accounted for by the Cole-Cole function (for the relaxation process) and an additional dc conductivity contribution (for the ionic charge transport). Moreover, to achieve reasonable fits we found it necessary to employ an additional contribution $\sigma' = \sigma_0 \omega^s$ with $s < 1$. This corresponds to the "universal dielectric response" (UDR) as suggested by Jonscher [25]. It is usually ascribed to hopping charge transport and often found in ionic conductors [32,33,34]. The fitting lines shown in Fig. 7 are from this approach leading to a reasonable description of the experimental spectra. The overall number of parameters involved in these fits is quite considerable, and thus one may worry about a possible correlation of parameters. However, depending on temperature, only part of these different assumed contributions had to be actually used for the fits. For examples, at high temperatures, the relaxation contribution obviously is shifted out of the frequency window and at the lowest temperatures the electrode contributions are negligible. Moreover, these fits only aim at the determination of the two most relevant parameters, the dc conductivity and the relaxation time. Both quantities can be also estimated by bare eye from the experimental spectra (see discussion above) and a comparison of fit and non-fit results confirms the significance of the deduced fit parameters (see also discussion below).

The σ_{dc} values resulting from the fits are included in Fig. 6b (closed circles). Their temperature dependence reasonably follows the behavior of $\sigma'(T)$ at the lowest frequency of 1 Hz, which is approached at high temperatures by all shown $\sigma'(T)$ curves and can be roughly identified by the dc conductivity in this plot as discussed above. In Fig. 8a, the σ_{dc} data are plotted using an Arrhenius representation, $\log_{10}(\sigma_{dc})$ vs. 1000/T. It reveals clear deviations from simple thermally-activated Arrhenius behavior, $\sigma_{dc} \propto \exp[-E_B/(k_B T)]$, which should appear linear in this plot. Only in a limited region at high temperatures σ_{dc} may be assumed to follow the Arrhenius law as indicated by the line in Fig. 8a. From its slope, an energy barrier value, $E_B = 0.49$ eV was determined at high temperatures above RT. On the other hand, the isosurface of BVEL mapped at $V_{pot} = -0.49$ eV at 393 K (Fig. 9a) is matched exactly to the *true* DDHBN (Fig. 4a) along which H$^+$ would retain optimal bond valence. Hence, it can be concluded that the long-range protonic dynamic disorder is responsible for the ionic dc conductivity at high temperatures above RT in rockbridgeite. At 298 K, in comparison, the isosurface of BVEL at $V_{pot} = -0.49$ eV around H1 sites (Fig. 9b) is isolated. Accordingly, a continuous conducting pathway over H1 sites cannot be formed at 298 K yet. This is indicative of locally limited motions of protons at site, as well as of their site-exchanging processes locally limited around HBs near and below RT. Such local motions require in general low activation energy, represented by the flat slope in an Arrhenius plot. Indeed, $\sigma_{dc}(T)$ obviously exhibits a complicated non-linear tendency (Fig. 8a), which may be associated with a superposition of the long-range protonic dynamics and fast local motions near RT. Vehicle-like site-exchanging protons along H3-H2-H2 around O5, as shown in Fig. 5, could be the relevant contribution to such a local charge transport process in rockbridgeite near RT.

Overall, our dielectric data provide rather clear evidence for ionic conductivity, with thermal activation over a barrier of 0.49 eV at high temperatures. However, at lower temperatures, $\sigma_{dc}(T)$ obviously crosses over into weaker temperature dependence (Fig. 8a). While in the Arrhenius-representation purely thermally activated behavior corresponds to a straight line, tunneling in principle would yield a nearly constant $\sigma_{dc}(T)$. Thus the temperature dependence of σ_{dc} shown in Fig. 8a can also be interpreted as a smooth transition from thermally-activated to tunneling-dominated charge transport with decreased
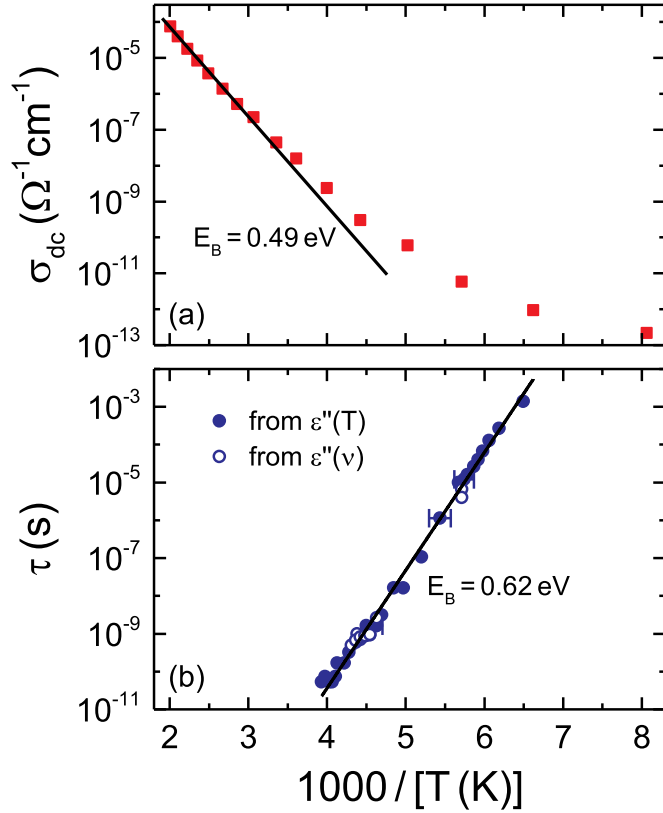
Fig. 8. Temperature dependence of the dc conductivity (a) and the reorientational relaxation time (b), both plotted in Arrhenius representation. In frame (b), results deduced from the temperature- and from the frequency-dependent data are shown (closed and open circles, respectively). The lines are linear fits; for σ_{dc} the fitting was applied to the highest temperatures only.

temperatures. When considering that the charge carriers indeed are H^+, tunneling seems reasonable for this smallest ionic species as the temperature dependence of σ_{dc} becomes dramatically weaker below 200 K (Fig. 8a).

It should be noted that for various metals (e.g., Nb and Ta [35]), the tunneling of hydrogen atoms is a well-known effect, where the H atoms are believed to move between interstitial sites of the metallic lattice. There, for the temperature-dependent hydrogen diffusion coefficients, pronounced non-Arrhenius behavior was found [35], roughly resembling the temperature-dependence of the conductivity documented in Fig. 8(a). It was theoretically explained by tunneling of hydrogen atoms, involving excited states and a phonon-assisted tunneling mechanism [36,37,38]. In the present case of rockbridgeite, the diffusion of protons which are not located at interstitial sites is detected. Thus, those theoretical approaches probably cannot be directly applied to our data from dielectric measurements. To further corroborate this tunneling scenario, future measurements of deuterated samples, for which considerably reduced tunneling probabilities are expected, would be helpful. For this purpose, however, we have to overcome difficulties in manufacturing pure samples of synthetic counterparts of rockbridgeite-type minerals.

What remains to be clarified is the microscopic origin of the detected relaxational process. The deduced temperature dependence of the relaxation time is shown in Fig. 8b, again using an Arrhenius representation. As explained above, these data were partly determined from temperature-dependent (Fig. 6) and partly from frequency-dependent representations of the experimental data (Fig. 7) and, in the latter case, both from fits and by simply reading off peak frequencies. Nevertheless, there is reasonable agreement of the different data sets, corroborating their reliability. The linear fit in Fig. 8b demonstrates

that the relaxation time follows Arrhenius behavior, $\tau = \tau_0 \exp[E_B/(k_B T)]$ in the whole temperature range of 150–250 K with an energy barrier of 0.62 eV. Notably, the obtained prefactor $\tau_0 \approx 10^{-23}$ s, representing an inverse attempt frequency which often is of the order of typical lattice vibrations, seems unreasonably small. This implies that, at higher temperatures, deviations from Arrhenius behavior may be expected as commonly found for glassy freezing [24,39,40]. A comparison of $\sigma_{dc}(1/T)$ and $\tau(1/T)$ in Fig. 8 immediately reveals significant decoupling of both dynamic quantities: $\tau(T)$ behaves thermally activated in a temperature region where clear deviations from Arrhenius behavior show up in $\sigma_{dc}(T)$ and the two energy barriers differ significantly. This indicates that the detected relaxation does not correspond to the process that is sometimes assumed to universally occur in ionic conductors and to be closely related to the global ionic charge transport [41,42,43]. Instead, the found relaxation is a separate process, not related to the proton hopping along the mentioned continuous HBs network. It seems natural to ascribe it to the local hopping of protons in well-defined double-well potentials [44,45], for which there are several possibilities within the structure of rockbridgeite. Notably, when considering that this local relaxational dynamics continuously slows down over many decades of frequency with decreasing temperature, in some respect this compound reminds of an orientational glass [46]. A similar freezing of proton dynamics was also found, e.g., in mixtures of betaine phosphate and betaine phosphite [45]. There the thermally-activated slowing down of local proton hopping was proposed to lead to a so-called "proton glass" state, as also known for the KH_2PO_4 family of compounds [46,47]. The orientational-glass temperature, deduced by extrapolating the Arrhenius fit in Fig. 8b to $\tau = 100$ s [24] is about 125 K.

4. Summary and conclusions

In summary, our thorough structural and dielectric studies of a rockbridgeite-type compound have revealed two essential results: First, there is strong evidence for ionic conductivity, thermally activated at high and possibly tunneling at low temperatures. The results are well compatible with proton conduction, i.e. global proton motion across the sample. The neutron scattering length distribution reconstructed by MEM and BVEL maps at 393 K clearly revealed a honeycomb-like path for protons conducting preferentially over H1 sites along the crystallographic **a** axis, well compatible with the energy barrier of 0.49 eV for ion hopping deduced from the dielectric results. The two statistically occupied H3 sites seem to be not directly involved in this long-range charge transport process, but relevant for local fast motions. The dc conductivity value of about 10^{-4} Ω^{-1} cm^{-1} at 500 K is an averaged magnitude, as evaluated from dielectric spectra direction-independently acquired with fine crystallites mass. In this sense, the protonic conductivity can be even higher in a rockbridgeite single crystal plate, oriented-cut perpendicular to the **a** axis. The charge transport by thermally activated OH and HOH groups in the title compound reminds of the conduction mechanism of protons in hydroxyapatite in which the proton diffusion and reorientation of hydroxide ions occur over complex sinusoidal paths wrapping the 2D HB network in the hexagonal channel [48].

Another relevant finding in the present study is the existence of a thermally activated dipolar relaxation process in this phosphatic oxy-hydroxide. We ascribe it to the local motion of protons confined within double-well potentials, most likely formed by the two statistically occupied H3 sites which form a short and almost stretched HB. This resembles the approach of a proton-glass state as detected in other materials [46]. This relaxational local proton dynamic disorder is well decoupled from the long-range proton dynamics leading to ionic conductivity. In the case of rockbridgeite, the detected extremely fast relaxational proton dynamic in a time domain of about 50 ps at about 250 K continuously slows down to about 1 ms at 150 K. The extrapolation of the relaxation time to lower temperatures points to an
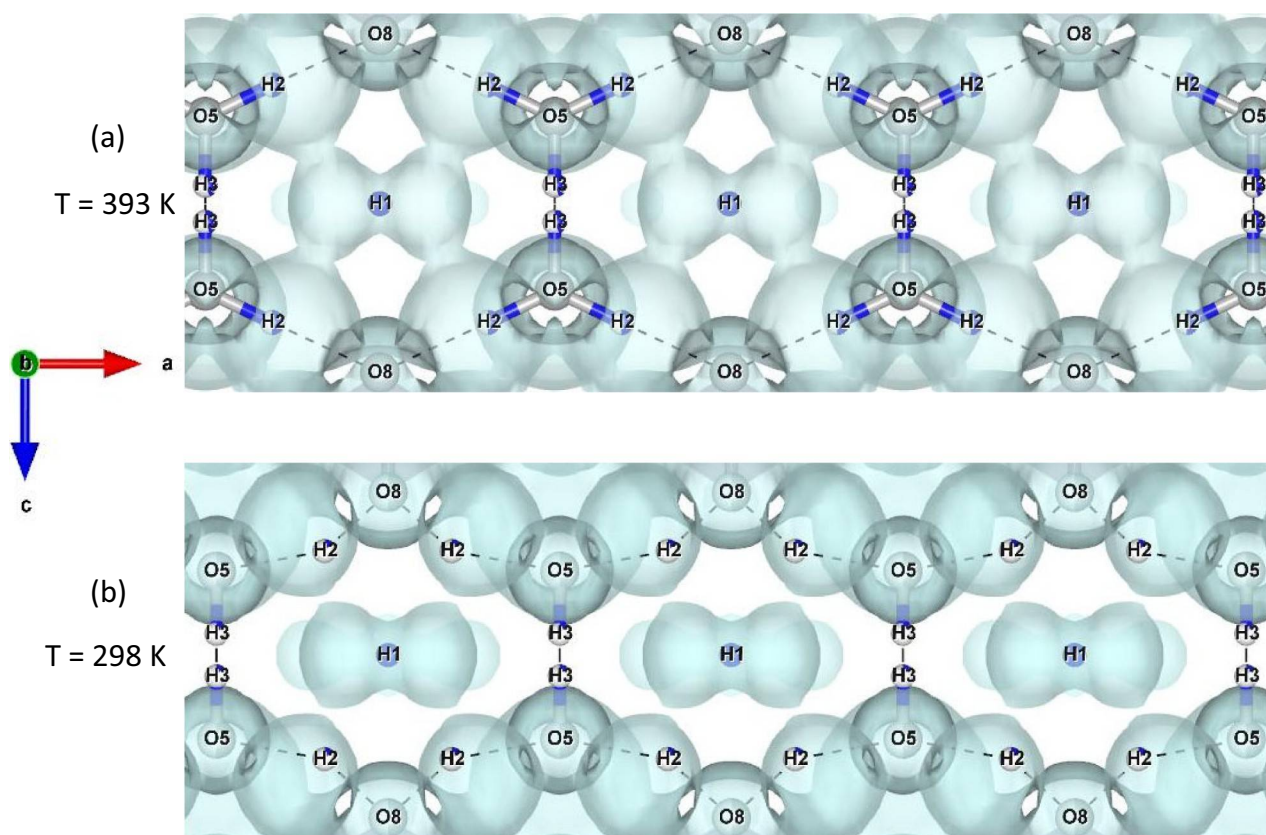
Fig. 9. BVEL Isosurface around H sites (in pale blue) with threshold at $V_{pot} = -0.49$ eV, evaluated with the structure model refined with HRNPD data of the title compound at 393 K (a) and 298 K (b). The *true* DDHB network over H1 sites is reflected to the BVEL completely at 393 K (a). (For interpretation of the references to colour in this figure legend, the reader is referred to the web version of this article.)

orientational proton-glass state below a glass-transition temperature of about 125 K, where $\tau(T)$ reaches 100 s.

Our previous [3] and current structure analyses with HRNPD data revealed that the only significant structural change occurring below the magnetic transition in this compound is the ordering of the protons at the H3 sites on a position just in the middle between the adjacent oxygen atoms. An extrapolation of the Arrhenius temperature-dependence of $\tau(T)$ (Fig. 8b) to the transition temperature of about 82 K shows that at this temperature the proton relaxation is completely frozen. Here all protons should be immobile and statistically distributed, being located on one minimum of the double-well potential formed by the two H3 sites. Obviously, below the structural/magnetic transition at 82 K, this double-well potential is replaced by a single potential minimum, enabling the protons to move from their off-center to a centered position.

Overall, the protonic dynamics cannot be realized in rockbridgeite-type compounds without collective motions of their OT framework polyhedra because OH and HOH groups form their ligands with oxygens. Recently, the evolution of three distinct phonons in an energy transfer range between -15 meV and -50 meV from 250 K to 400 K could be detected in quasi-elastic neutron scattering (QENS). For assignments of these phonon energies, an extensive theoretical work is in progress. The time and length scales for fast proton dynamics in several ps could be determined from QENS, as well. Relevant findings from QENS will be reported elsewhere.

Author statement

All authors have seen and approved the final version of the manuscript being submitted.

Declaration of competing interest

The authors declare that they have no known competing financial interests or personal relationships that could have appeared to influence the work reported in this paper.

References

[1] F.C. Hawthorne, Mineral. Magaz. 62 (2) (1998) 141–164.
[2] S.M. Mattson, G.R. Rossmann, Phys. Chem. Minerals 14 (1987) 94–99.
[3] B. Röska, S.-H. Park, D. Behal, K.-U. Hess, A. Günther, G. Benka, C. Pfleiderer, M. Hoelzel, T. Kimura, J. Phys. Condens. Matter 30 (2018) 235401 12pp.
[4] A. Hartl, S.-H. Park, M. Hoelzel, N. Paul, R. Gilles, J. Solid St. Chem. 277 (2019) 290–302.
[5] W. Münich, K.-D. Kreuer, U. Traub, J. Maier, J. Mol. Struct. (THEOCHEM) 381 (11996).
[6] B.V. Merinov, Solid St. Ionics 84 (1996) 89–96.
[7] K.-D. Kreuer, S.J. Paddison, E. Spohr, M. Schuster, Chem. Rev. 104 (2004) 4637–4678.
[8] G.J. Redhammer, G. Roth, G. Tippelt, M. Bernroider, W. Lottermoser, G. Amthauer, R. Hochleitner, Acta Cryst C62 (2006) 24–28.
[9] P.B. Moore, Am. Mineral. 55 (1–2) (1970) 135–169.
[10] M. Hoelzel, A. Senyshyn, N. Juenke, H. Boysen, W. Schmahl, H. Fuess, Nucl. Inst. Meth. Phys. Research A667 (2012) 32–37.
[11] V. Petrícek, M. Dušek, L. Palatinus, Z. Kristallogr. 229 (5) (2014) 345–352.
[12] D.M. Collins, Nature 298 (1982) 49–51.
[13] J. Nocedal, Math. Comput. 35 (1980) 773–782.
[14] K. Momma, T. Ikeda, A.A. Belik, F. Izumi, Powder Diffract. (2013) 1–10.
[15] S. Adams, Solid St. Ionics 177 (2006) 1625–1630.
[16] S. Adams, R.P. Rao, Phys. Status Solidi A 208 (8) (2011) 1746–1753.
[17] I.D. Brown, IUCr Monographs on Crystallography 12, Oxford University Press, 2002.

[18] J. Rodriguez-Carvajal, Physica B 192 (1–2) (1993) 55–69.
[19] K. Momma, F. Izumi, J. Appl. Crystallogr. 41 (2008) 653–658.
[20] R. Böhmer, M. Maglione, P. Lunkenheimer, A. Loidl, J. Appl. Phys. 65 (1989) 901.
[21] S. Emmert, M. Wolf, R. Gulich, S. Krohns, P. Lunkenheimer, A. Loidl, Eur. Phys. J. B 83 (2011) 157.
[22] P. Lunkenheimer, V. Bobnar, A.V. Pronin, A.I. Ritus, A.A. Volkov, A. Loidl, Phys. Rev. B 66 (2002) 052105.
[23] F. Kremer, A. Schönhals (Eds.), See collection of articles in *Broadband Dielectric Spectroscopy*, Springer, Berlin, 2002.
[24] P. Lunkenheimer, A. Loidl, F. Kremer, A. Loidl (Eds.), The Scaling of Relaxation Processes, Springer, Cham, 2018, p. 23.
[25] A.K. Jonscher, Dielectric Relaxation in Solids, Chelsea Dielectrics Press, London, 1983.
[26] P. Lunkenheimer, A. Loidl, J. Phys. Condens. Matter 27 (2015) 373001.
[27] P. Lunkenheimer, R. Fichtl, S.G. Ebbinghaus, A. Loidl, Phys. Rev. B 70 (2004) 172102.
[28] P. Lunkenheimer, S. Krohns, S. Riegg, S.G. Ebbinghaus, A. Reller, A. Loidl, Eur. Phys. J. Special Topics 180 (2010) 61.
[29] S. Havriliak, S.S. Negami, Polymer 8 (1967) 161.
[30] K.S. Cole, R.H. Cole, J. Chem. Phys. 9 (1941) 341.
[31] P. Sippel, P. Lunkenheimer, S. Krohns, E. Thoms, A. Loidl, Sci. Rep. 5 (2015) 13922.

[32] S.R. Elliott, Phil. Mag. B 60 (1989) 777.
[33] K. Funke, Phil. Mag. A 68 (1993) 711.
[34] A. Pimenov, P. Lunkenheimer, H. Rall, R. Kohlhaas, A. Loidl, R. Böhmer, Phys. Rev. E 54 (1996) 676.
[35] Z. Qi, J. Volkl, R. Lasser, H. Wenzl, J. Phys. F 13 (1983) 2053.
[36] H.R. Schober, A.M. Stoneham, Phys. Rev. Lett. 60 (1988) 2307.
[37] S. Dattagupta, H.R. Schober, Phys. Rev. B 57 (1998) 7606.
[38] P.G. Sundell, G. Wahnström, Phys. Rev. B 70 (2004) 224301.
[39] M.D. Ediger, C.A. Angell, S.R. Nagel, J. Phys. Chem. 100 (1996) 13200.
[40] J.C. Dyre, Rev. Mod. Phys. 78 (2006) 953.
[41] P.B. Macedo, C.T. Moynihan, R. Bose, Phys. Chem. Glasses 13 (1972) 171.
[42] J.C. Dyre, J. Appl. Phys. 64 (1988) 2456.
[43] D.L. Sidebottom, Rev. Mod. Phys. 81 (2009) 999.
[44] E. Courtens, Phys. Rev. Lett. 52 (1984) 69.
[45] S.L. Hutton, I. Fehst, R. Böhmer, M. Braune, B. Mertz, P. Lunkenheimer, A. Loidl, Phys. Rev. Lett. 66 (1991) 1990.
[46] U.T. Hochli, K. Knorr, A. Loidl, Adv. Phys. 39 (1990) 405.
[47] Y. Feng, C. Ancona-Torres, T.F. Rosenbaum, G.F. Reiter, D.L. Price, E. Courtens, Phys. Rev. Lett. 97 (2006) 145501.
[48] M. Yashima, N. Kubo, K. Omoto, H. Fujimori, K. Fujii, K. Ohoyama, J. Phys. Chem. C 118 (2014) 5180–5187.